

Article

# Effect of TiO<sub>2</sub> on the Sintering Behavior of Chromium-Bearing Vanadium–Titanium Magnetite

Weidong Tang <sup>1</sup> , Songtao Yang <sup>1,2</sup>, Gongjin Cheng <sup>1</sup>, Zixian Gao <sup>1</sup>, He Yang <sup>1</sup> and Xiangxin Xue <sup>1,\*</sup>

<sup>1</sup> School of Metallurgy, Northeastern University, Shenyang 110819, China; twdking@163.com (W.T.); yangsongtao1984@163.com (S.Y.); chenggj1985@126.com (G.C.); gaozixian1992@163.com (Z.G.); 1610473@stu.neu.edu.cn (H.Y.)

<sup>2</sup> School of Materials and Metallurgy, University of Science and Technology Liaoning, Anshan 114051, China

\* Correspondence: xuexx@mail.neu.edu.cn

Received: 6 May 2018; Accepted: 20 June 2018; Published: 23 June 2018



**Abstract:** The sintering pot test was used to investigate the effect of TiO<sub>2</sub> on the sintering behavior of chromium-bearing vanadium–titanium magnetite (CVTM) sinter. The main characterization methods of X-ray fluorescence (XRF), X-ray diffraction (XRD), scanning electron microscopy-energy disperse spectroscopy (SEM-EDS), and metallographic microscopy were employed. In this study, yield, tumbler index (TI), vertical sintering speed, productivity, reduction degradation index (RDI), and reduction index (RI) were tested and calculated. The yield first increases from 82.87% to 84.37% and then decreases to 83.65%, vertical sintering speed first increases from 17.00 mm·min<sup>-1</sup> to 23.45 mm·min<sup>-1</sup> and then decreases to 20.61 mm·min<sup>-1</sup>, and productivity first increases from 2.33 t·m<sup>-2</sup>·h<sup>-1</sup> to 3.14 t·m<sup>-2</sup>·h<sup>-1</sup> and then decreases to 2.69 t·m<sup>-2</sup>·h<sup>-1</sup> with increasing TiO<sub>2</sub> content. The TI increases from 45.81% to 52.09%, and RDI increases from 74.99% to 96.74%, while RI decreases from 67.92% to 47.15% with increasing TiO<sub>2</sub> content.

**Keywords:** titanium dioxide; chromium-bearing vanadium–titanium magnetite; sinter; sintering behavior

## 1. Introduction

Chromium-bearing vanadium–titanium magnetite (CVTM) iron ore containing Fe, Ti, Cr, and V is a special and valuable iron ore as known by the exploitation of vanadium–titanium magnetite (VTM), ilmenite, and chromite [1,2]. As a kind of valuable iron ore resource, Hongge CVTM is found in the Panzhihua area in China. Similar types of ores are mainly distributed in Russia, Canada, Australia and other places [3,4]. As it is known, many studies have been done for the ordinary VTM, while the studies on CVTM with complex phase compositions and different properties are scarce [5,6]. Owing to the immature production technology of CVTM in the blast furnace (BF) process, the abundant quantity of such CVTM has not been exploited and efficiently used on a large scale. Therefore, it is of great importance to study the utilization of the special iron ore.

In order to use CVTM efficiently, the sintering behaviors of CVTM have been proposed by the authors' laboratory [7–9]. In the BF process, the CVTM sinter with different basicity, coke ratios, and MgO contents have been studied. Yang [7,8] studied the effects of coke ratios and MgO on the sintering behaviors and the metallurgical properties of CVTM. Yang [9] surveyed the effect of basicity on the mineral compositions and elements migration of CVTM sinters. Particularly, titanium is one of the main valuable elements in CVTM, and titanium has an important influence on sintering properties. However, the contents of TiO<sub>2</sub> in these studies were lower than 2 wt %, and the sintering behaviors with the relatively higher content of TiO<sub>2</sub> have not been studied comprehensively in the past. Therefore, the

sintering behaviors of CVTM with high  $\text{TiO}_2$  contents are necessary to be researched, and it is of great importance to carry out in this work.

As part of continuing work to study the utilization of CVTM in the BF process, the effect of  $\text{TiO}_2$  on sintering behavior of CVTM was explored in this paper. First, the yield, tumbler index (TI), vertical sintering speed, productivity, reduction degradation index (RDI), and reduction index (RI) were tested and calculated. The mineral compositions and microstructures of CVTM sinter with different  $\text{TiO}_2$  contents were then studied. These results will provide theoretical and technical bases for the effective production of the CVTM sinter and facilitate its exploitation.

## 2. Materials and Methods

### 2.1. Raw Materials and Characterisation Methods

Hongge CVTM originates from the Panzhihua area in China. Ordinary magnetite (OM), gas-ash (GA), magnetic powder (MP), return mine (RM), lime, coke, and coal were supplied by Chengde Jianlong Iron and Steel Group Company (Chengde, China).

The X-ray fluorescence (XRF, ZSXPrimus II; Rigaku, Tokyo, Japan) was used to test the chemical compositions of raw materials. The X-ray diffraction (XRD, X' Pert Pro; PANalytical, Almelo, The Netherlands) with  $\text{Cu K}\alpha$  radiation (wavelength = 1.5406 Å) at a setting of 40 kV and 40 mA was used to analyze the mineral phases of CVTM and CVTM sinters. The scanned range was  $2\theta = 5\text{--}90^\circ$  with a step of  $2\theta = 0.17^\circ$  and 1 s-step<sup>-1</sup>. All of the tested powders were ground to lower than 200 μm. The scanning electron microscope (SEM, Ultra Plus; Carl Zeiss GmbH, Jena, Germany) was used to detect the microstructure of reductive CVTM sinters, and backscattering detector (BSE) was used to investigate sinter surface, and energy disperse spectroscopy (EDS) was used to acquire mineral compositions. Sinter sample was heat mounted in resin and polished by mirror finish for microstructure and mineralogy analysis. A metallographic microscope (Leica DM1750M; Leica, Cambridge, UK) was used to detect the mineralogy of CVTM sinter.

### 2.2. Experiments

Figure 1 shows the granulating process of CVTM sinter materials. Figure 2 shows the schematic of sinter pot test equipment including operation cabinet, gas supply, gas burner, sinter pot, data acquisition, dust extraction, and draft fan. Table 1 shows the sintering parameters of sintering pot test. Table 2 shows the experimental scheme and ingredient of sinter materials. The  $\text{TiO}_2$  content changes with the addition of ilmenite. First, 100 kg raw materials with 4.05% fuel (coke:coal = 1) are mixed in a mixer and granulated in a granulator for 10 min, and rotation angle of granulator is in the range of  $\pm 45^\circ$  at the process of granulation as shown in Figure 1. Then, the pelletized sinter materials are filled in sinter pot with a diameter of 320 mm and a height of 700 mm, and 20 g coke is sprinkled evenly on the surface of sinter materials for ignition. Then, liquefied natural gas is lit and used to ignite the sinter materials at an ignition temperature of 1050 °C, and ignition suction is 8.00 kPa. At the end of ignition, the extraction fan was started up to make sinter suction at 12.00 kPa. Finally, the temperature of flue gas reaches the peak value, and sinter temperature begins downturn. When the temperature of flue gas is below 100 °C, sintering pot test finishes, and dust extraction fan starts up to eliminate the dust in sinter broken process. The properties of TI, particle size distribution, RDI, and RI were determined according to ISO-3271, ISO-4701, ISO-4696, and ISO-7215, respectively.

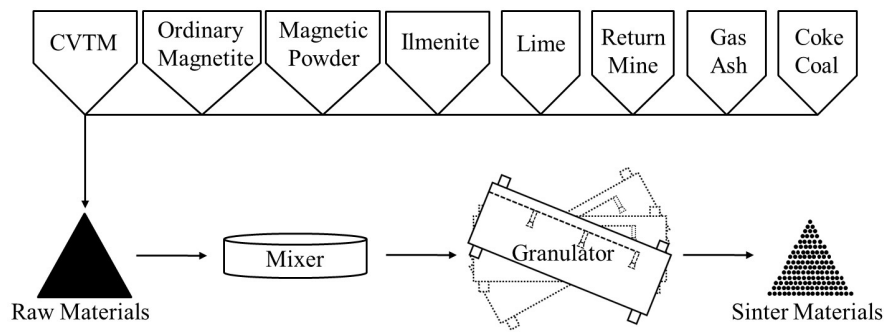


Figure 1. Granulating process of vanadium–titanium magnetite (CVTM) sinter materials.

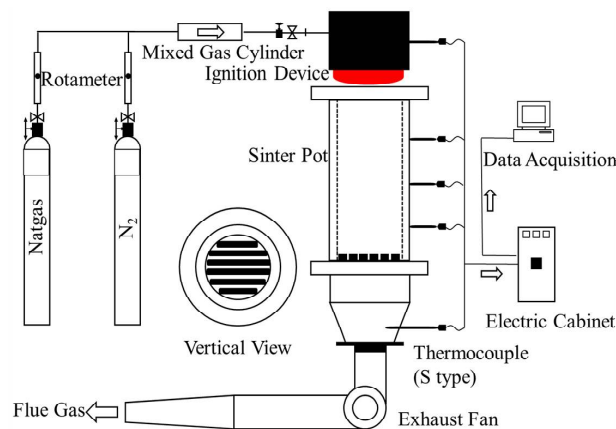


Figure 2. Schematic of sinter pot test equipment.

Table 1. Parameters of CVTM sintering pot test.

Item	Parameter	Item	Parameter
Sinter pot height	700 mm	Sinter pot inner diameter	320 mm
Sintering weight	100 kg	Pelletizing time	10 min
Ignition temperature	1050 °C	Ignition time	2 min
Height of grate layer	20 mm	Moisture	8.5 ± 0.5%
Ignition pressure	8.00 kPa	Exhausting pressure	12.0 kPa

Table 2. Experimental scheme and ingredient of sinter materials (wt %).

Number	$\omega(\text{TiO}_2)$	Mixed Sinter Raw Materials						
		CVTM	OM <sup>1</sup>	RM <sup>2</sup>	GA <sup>3</sup>	MP <sup>4</sup>	Lime	Ilmenite
1	5.85	35.9	30	20	1	1	12.2	0
2	7.35	30.9	30	20	1	1	12.4	4.8
3	8.85	26.7	30	20	1	1	12.4	8.9
4	10.35	22.9	30	20	1	1	12.8	12.3
5	11.85	19.5	30	20	1	1	12.9	15.6

<sup>1</sup> Ordinary magnetite. <sup>2</sup> Return mine. <sup>3</sup> Gas-ash. <sup>4</sup> Magnetic powder.

### 2.3. Definition of Parameters

#### 2.3.1. Productivity

The productivity of sinter is an important indicator to measure the production capacity of sintering production. The calculation equation of productivity is given in Equation (1):

$$P = \frac{M \cdot Y}{A \cdot t} \quad (1)$$

where  $P$  is the unit productivity ( $\text{t} \cdot \text{m}^{-2} \cdot \text{h}^{-1}$ ),  $M$  is the mass of product sinters (t),  $Y$  is the yield of product sinters (%),  $A$  is the effective sintering area of sinter pot ( $\text{m}^2$ ), and  $t$  is the sintering time (h).

### 2.3.2. Reduction Degradation Index

The RDI is a measure of disintegration property of iron ore sinter on the reduction reaction with CO at 500 °C. The RDI reflects the BF in the upper stack regions where it is mildly reducing, and temperatures are low [10]. The particle sizes (+6.3 mm, +3.15 mm, −0.5 mm) of sinter after reduction are used to calculate the RDI. The standard of ISO-4696,  $\text{RDI}_{+6.3}$  represents the reduction intensity of iron ore sinter, and  $\text{RDI}_{+3.15}$  represents the RDI, and  $\text{RDI}_{-0.5}$  reflects the attrition strength of iron ore sinter after reduction. The equations of RDI are given in Equations (2)–(4):

$$\text{RDI}_{+6.3} = \frac{m_{D1}}{m_{D0}} \times 100 \quad (2)$$

$$\text{RDI}_{+3.15} = \frac{m_{D1} + m_{D2}}{m_{D0}} \times 100 \quad (3)$$

$$\text{RDI}_{-0.5} = \frac{m_{D0} - (m_{D1} + m_{D2} + m_{D3})}{m_{D0}} \times 100 \quad (4)$$

where  $m_{D0}$  is the sinter weight after the reduction (g),  $m_{D1}$  is the weight of sinter on the 6.3 mm sieve (g),  $m_{D2}$  is the weight of sinter on the 3.15 mm sieve (g), and  $m_{D3}$  is the weight of sinter on the 0.5 mm sieve (g).

### 2.3.3. Reduction Index

The RI of sinter is based on the standard ISO-7215, and it shows the reduction conditions of sinter in BF at 900 °C. The RI of sinter is calculated via Equation (5):

$$X_t = \left[ \frac{0.111\omega(\text{FeO})}{0.430\omega(\text{TFe})} + \frac{m_1 - m_2}{m_1 \times 0.430\omega(\text{TFe})} \right] \times 100\% \quad (5)$$

where  $X_t$  is the RI of CVTM sinter at time  $t$  (%),  $\omega(\text{FeO})$  and  $\omega(\text{TFe})$  are the mass of FeO and total iron of CVTM sinter before reduction (%);  $m_1$  and  $m_2$  are the mass of CVTM sinter before reduction (g).

## 3. Results and Discussion

### 3.1. Chemical Assays and Characterisation

The chemical compositions of raw materials are shown in Table 3. The coke and coal breeze and chemical compositions are shown in Table 4. Table 5 shows the size distribution of CVTM, and it indicates the particle size lower than 75  $\mu\text{m}$  occupies 72.47%, which indicates the CVTM ore is appropriate for granulation.

**Table 3.** Chemical compositions of raw materials (wt %).

Item	TFe	FeO	TiO <sub>2</sub>	V <sub>2</sub> O <sub>5</sub>	Cr <sub>2</sub> O <sub>3</sub>	CaO	SiO <sub>2</sub>	MgO	Al <sub>2</sub> O <sub>3</sub>	P	S
CVTM	53.35	26.91	11.60	0.57	0.81	0.96	4.71	3.33	2.82	0.02	0.26
OM	63.79	28.35	0.89	0.06	0.02	0.38	7.15	0.38	1.25	0.02	0.05
Ilmenite	34.65	17.93	45.12	0.36		0.79	4.93	1.02	0.89	0.02	0.01
GA	32.39		1.79	0.25	0.16	5.16	5.95	1.79	2.69	0.07	0.17
MP	0.14		0.03			29.4	2.58	20.65	0.90		
lime						60.80	3.42	2.87	1.11		

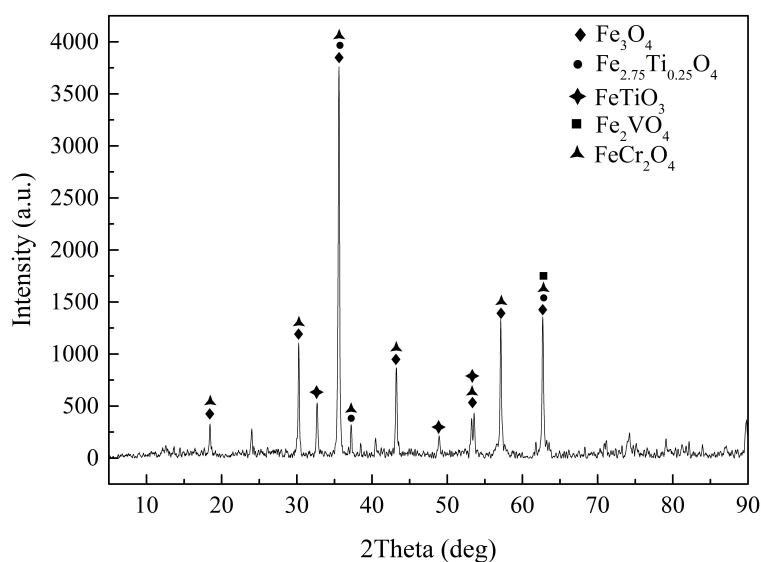
**Table 4.** Industrial analysis of coke breeze and chemical compositions of the ash (wt %).

Item	Fixed Carbon	Volatile	Organic Compounds	Ash					$\Sigma$
				CaO	SiO <sub>2</sub>	MgO	Al <sub>2</sub> O <sub>3</sub>	Others	
Coke	76.90	0.559	1.48	1.35	6.4	0.28	4.18	8.85	100.00
Coal	85.40	0.147	1.35	0.74	4.6	0.18	3.35	4.23	100.00

**Table 5.** Size distribution of CVTM (wt %).

−38 $\mu\text{m}$	38–45 $\mu\text{m}$	45–53 $\mu\text{m}$	53–75 $\mu\text{m}$	75–150 $\mu\text{m}$	+150 $\mu\text{m}$
44.55	7.88	15.73	4.31	21.21	5.82

Figure 3 shows the XRD pattern of CVTM, and the CVTM primarily consists of magnetite ( $\text{Fe}_3\text{O}_4$ ), titanomagnetite ( $\text{Fe}_{2.75}\text{Ti}_{0.25}\text{O}_4$ ), ilmenite ( $\text{FeTiO}_3$ ), coulsonite ( $\text{Fe}_2\text{VO}_4$ ) and chromite ( $\text{FeCr}_2\text{O}_4$ ). The inorganic crystal structure database (ICSD) card numbers of phases in CVTM are shown in Table 6.

**Figure 3.** XRD pattern of CVTM ore.**Table 6.** ICSD card numbers of phases in CVTM.

No.	Phase	Chemical Formula	ICSD No.
1	Magnetite	$\text{Fe}_3\text{O}_4$	79-0418
2	Titanomagnetite	$\text{Fe}_{2.75}\text{Ti}_{0.25}\text{O}_4$	75-1373
3	Ilmenite	$\text{FeTiO}_3$	75-0519
4	Coulsonite	$\text{Fe}_2\text{VO}_4$	75-1519
5	Chromite	$\text{FeCr}_2\text{O}_4$	34-0140
6	Hematite	$\text{Fe}_2\text{O}_3$	33-0664
7	Perovskite	$\text{CaTiO}_3$	88-0228
8	Kirschsteinite	$\text{CaFeSiO}_4$	34-0098
9	Fayalite	$\text{Fe}_2\text{SiO}_4$	76-0512
10	Magnesium ferrite	$\text{MgFe}_2\text{O}_4$	17-0464
11	Magnesium titanate	$\text{MgTiO}_3$	06-0494
12	Metallic iron	Fe	87-0721
13	Wustite	FeO	74-1880
14	Maghemite	$\gamma\text{-Fe}_2\text{O}_3$	79-1741
15	Titanium monoxide	TiO	86-2352
16	Spinel	$\text{Mg}_2\text{TiO}_4$	87-1173
17	Titanomagnetite	$\text{Fe}_{2.5}\text{Ti}_{0.5}\text{O}_4$	75-1375
18	Titanomaghemite	$\text{Fe}_{0.23}(\text{Fe}_{1.95}\text{Ti}_{0.42})\text{O}_4$	84-1595

### 3.2. Effect of TiO<sub>2</sub> on the Properties of CVTM Sinters

Figure 4 shows the XRD patterns of CVTM sinters with different TiO<sub>2</sub> content. The main phases of CVTM sinter are magnetite, hematite (Fe<sub>2</sub>O<sub>3</sub>), perovskite (CaTiO<sub>3</sub>), coulsonite, and chromite. The peak intensity of perovskite becomes stronger with increasing TiO<sub>2</sub> content, where the kirschsteinite (CaFeSiO<sub>4</sub>) generates with a TiO<sub>2</sub> content higher than 7.35% and transforms to fayalite (Fe<sub>2</sub>SiO<sub>4</sub>) when the TiO<sub>2</sub> content increases to 11.85%. Meanwhile, the magnesium ferrite (MgFe<sub>2</sub>O<sub>4</sub>) generates with a TiO<sub>2</sub> content higher than 7.35% and generates magnesium titanate (MgTiO<sub>3</sub>) with a TiO<sub>2</sub> content higher than 10.35%. The ionic radii of Mg<sup>2+</sup> (0.78 Å) and Fe<sup>2+</sup> (0.83 Å), as well as Ca<sup>2+</sup> (0.99 Å) and Mg<sup>2+</sup> (0.78 Å) are similar. Therefore, Mg<sup>2+</sup> enters the Fe<sub>3</sub>O<sub>4</sub> lattice to generate MgFe<sub>2</sub>O<sub>4</sub>, and Mg<sup>2+</sup> enters the CaTiO<sub>3</sub> lattice to generate MgTiO<sub>3</sub>. The ICSD card numbers of phases in CVTM sinters are shown in Table 6.

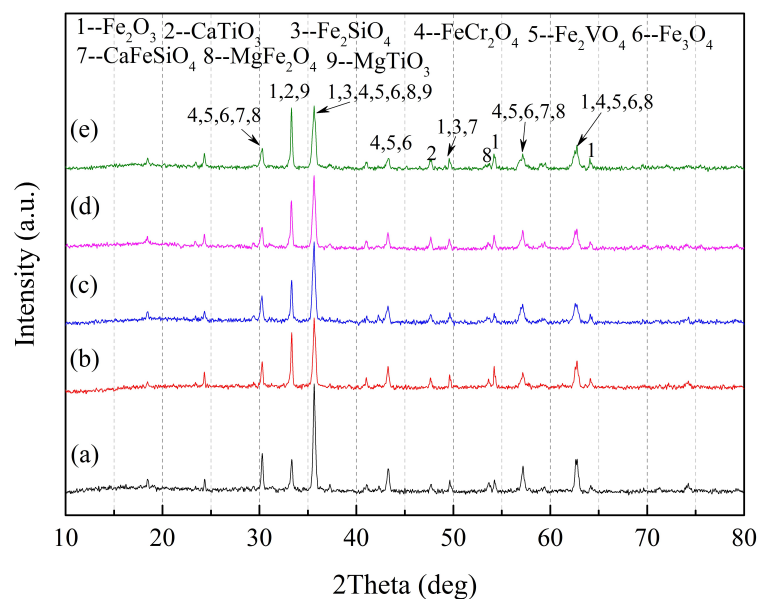


**Figure 4.** XRD pattern of CVTM sinter with different TiO<sub>2</sub> content. (a) TiO<sub>2</sub> = 5.85%; (b) TiO<sub>2</sub> = 7.35%; (c) TiO<sub>2</sub> = 8.85%; (d) TiO<sub>2</sub> = 10.35%; (e) TiO<sub>2</sub> = 11.85%.

The properties of CVTM sinter with different TiO<sub>2</sub> content are shown in Figure 5. The vertical sinter speed of CVTM sinter first increases and then decreases with increasing TiO<sub>2</sub> from 5.85% to 11.85%. The maximum value of sinter speed is 23.45 mm·min<sup>-1</sup> when TiO<sub>2</sub> content reaches 10.35%, as shown in Figure 5. In the sintering process, the oxidation reaction of magnetite and formation of liquid phase take place at low temperatures, while the ilmenite and titanomagnetite react with CaO, and generate perovskite with the addition of ilmenite under high temperature. By thermomechanical analysis, perovskite has an earlier generation than liquid phase of calcium ferrite.

Figure 5 shows the effect of TiO<sub>2</sub> on yield and TI of CVTM sinter. It shows that the yield increases from 82.87% to 84.37%, which then drops to 83.65%, and TI increases from 45.81% to 52.09% with increasing TiO<sub>2</sub> content. However, the results of yield and TI are different from previous findings where the TiO<sub>2</sub> has a negative effect on the crystal boundaries [11]. The productivity increases with increasing TiO<sub>2</sub> content and reaches a peak value of 3.14 t·m<sup>-2</sup>·h<sup>-1</sup>. From the microstructural analysis of the CVTM sinter as shown in Figure 6, the relatively concentrated silicate bonding phases exist as connection phases among crystals of magnetite and hematite, and perovskite phases exist in silicate phase as the form of crystallization [12,13]. Moreover, the hematite phases develop as crystals, and some detached hematite and magnetite phases are connected by the silicate and calcium ferrite. Hence, the silicate phases play essential roles in the bonding phase of CVTM sinter. Additionally, perovskite has a thermodynamic generation advantage compared with calcium ferrite, which is the initial melt in iron ore sintering process [14], and calcium ferrite is beneficial to the compressive strength of sinters [13]. When the TiO<sub>2</sub> content increases

to 11.85%, the calcium ferrite phases exist on the silicate phase, and the high strength of calcium ferrite enhances the strength of silicate bonding phases. With the analysis of the mineral content of CVTM sinter, the stable magnetite increases, and the glass phase decreases with increasing TiO<sub>2</sub> content. Combined with the XRD pattern of CVTM sinter, the volume expansion of sinter alleviates the cooling process due to the stable phases magnetite and magnesium ferrite.

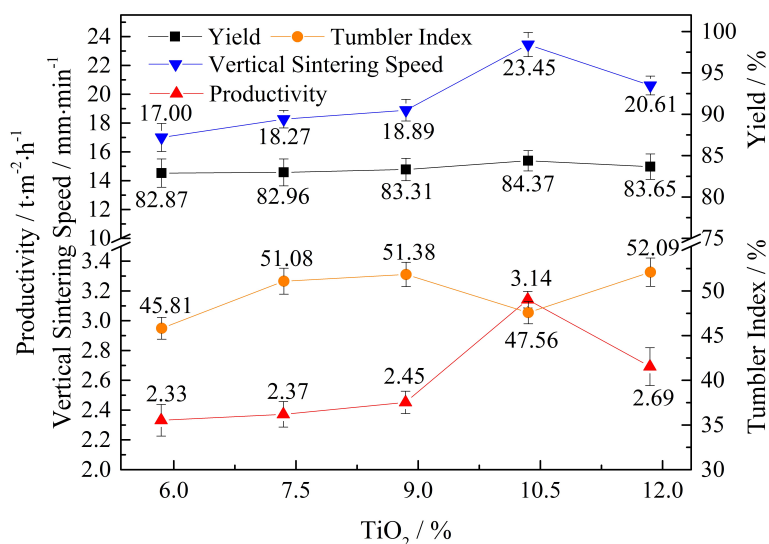


Figure 5. Properties and strength of CVTM sinter with different TiO<sub>2</sub> content.

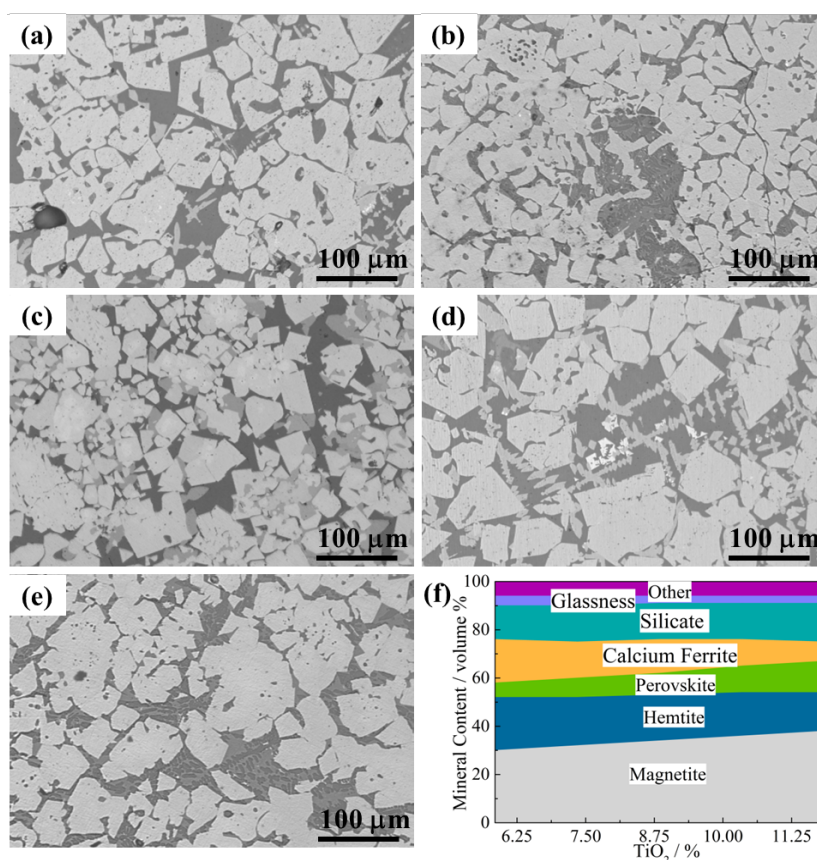


Figure 6. Microstructure of CVTM sinter with different TiO<sub>2</sub> content. (a) TiO<sub>2</sub> = 5.85%; (b) TiO<sub>2</sub> = 7.35%; (c) TiO<sub>2</sub> = 8.85%; (d) TiO<sub>2</sub> = 10.35%; (e) TiO<sub>2</sub> = 11.85%; (f) Mineral content.

Figure 7 shows the particle size distribution of CVTM sinters with different  $\text{TiO}_2$  content. When  $\text{TiO}_2$  content is 5.85%, the particle size distribution of sinter focuses on the size less than 16 mm and occupies 62%. When  $\text{TiO}_2$  content increases from 7.35% to 11.85%, the particle size distribution of sinter focuses on the size greater than 16 mm and occupies over 63%. The characteristics of particle size distribution of CVTM sinter indicates the improvement of sinter strength with increasing  $\text{TiO}_2$  content. Although the perovskite has low compression strength in iron ore sinters, perovskite has high wear resistance and hardness [15]. Therefore, the particle size distribution of CVTM sinter focuses on large particles.

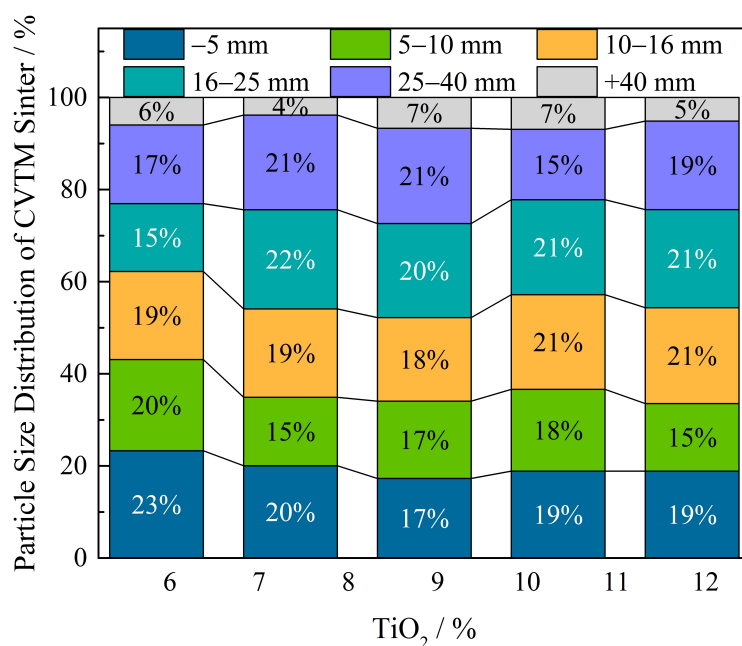


Figure 7. Particle size distribution of CVTM sinters with different  $\text{TiO}_2$  content.

The RDI and reduction intensity ( $\text{RDI}_{+6.3}$ ) increase with increasing  $\text{TiO}_2$  content, while the attrition strength ( $\text{RDI}_{-0.5}$ ) decreases as shown in Figure 8. In the upper stack regions of BF, the principal reduction reaction is the phase transformation of hematite to magnetite in sinter at  $400\text{ }^\circ\text{C}$ – $600\text{ }^\circ\text{C}$ . The primary cause of RDI is thought to be a crystalline transformation from rhombohedral hematite to cubic magnetite [16]. The anisotropic dimension varies because the change of crystal form results in severe stresses in specific planes and cracks in the brittle matrix [17]. Bristow et al. [18] found that  $\text{TiO}_2$ -containing glass phase in sinter structure had further increased the severity of crack propagation during reduction, and resulted in higher RDI of sinter. From the analysis of the microstructure of the CVTM sinter with different  $\text{TiO}_2$  content, the structural stress decreases due to the homogeneous phase structure. With the decreasing content of the hematite and glass phases, the variation of the stress decreases in the low reduction temperature. Meanwhile, the crystallization of perovskite phases mainly exists in the silicate phases as the form of solid-solution, and the perovskite has little effect on bonding phase of silicate and crystal strength between hematite and magnetite. Moreover, the magnesium ferrite exists between the intervals of hematite and magnetite, and magnesium ferrite has a suppressing effect on the reduction of hematite [19]. Hence, the RDI of CVTM sinter is well improved, and the permeability of lumpy zones could be improved with the application of CVTM sinter on BF.

Figure 9 shows the XRD patterns of reductive CVTM sinters with different  $\text{TiO}_2$  content at  $900\text{ }^\circ\text{C}$ . The main phases of reductive CVTM sinter are metallic iron (Fe), wustite (FeO), maghemite ( $\gamma\text{-Fe}_2\text{O}_3$ ), perovskite, coulsonite, magnesium ferrite, and titanium monoxide (TiO). The peak intensity of perovskite, wustite, and titanium monoxide become stronger with increasing  $\text{TiO}_2$  content, where the hematite disappears while magnetite generates with  $\text{TiO}_2$  higher than 7.35%. A new spinel phase

Mg<sub>2</sub>TiO<sub>4</sub> forms with TiO<sub>2</sub> higher than 10.35%, and new phases titanomagnetite (Fe<sub>2.5</sub>Ti<sub>0.5</sub>O<sub>4</sub>) and titanomaghemite (Fe<sub>0.23</sub>(Fe<sub>1.95</sub>Ti<sub>0.42</sub>)O<sub>4</sub>) form when TiO<sub>2</sub> content increases to 11.85%. The ICSD card numbers of phases in reductive CVTM sinters are shown in Table 6.

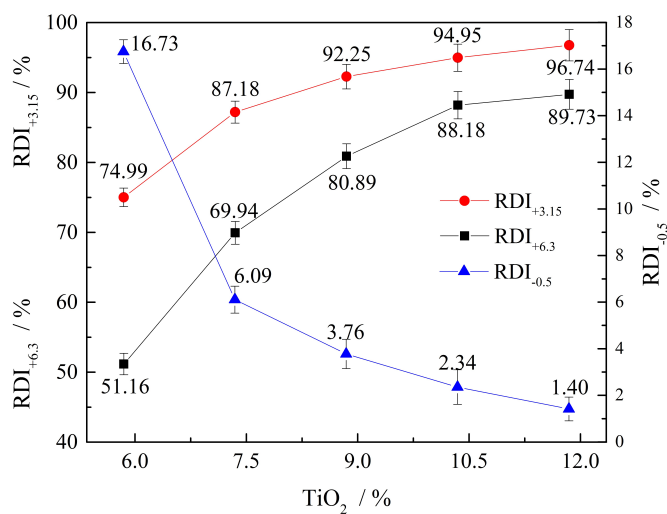


Figure 8. RDI of CVTM sinters with different TiO<sub>2</sub> content.

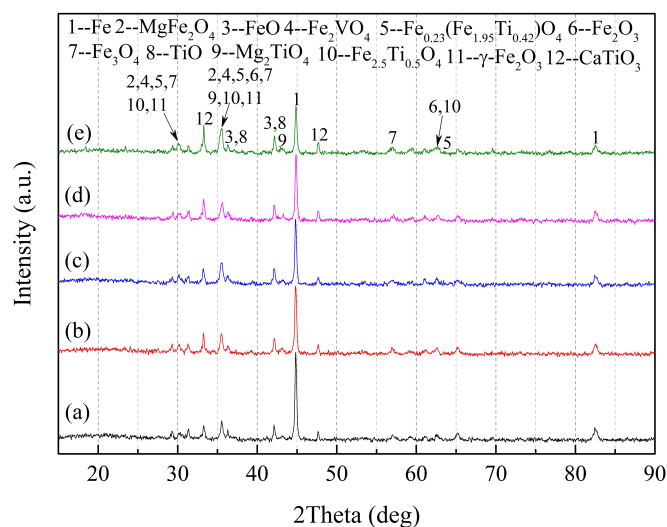


Figure 9. XRD pattern of reductive CVTM sinters with different TiO<sub>2</sub> content. (a) TiO<sub>2</sub> = 5.85%; (b) TiO<sub>2</sub> = 7.35%; (c) TiO<sub>2</sub> = 8.85%; (d) TiO<sub>2</sub> = 10.35%; (e) TiO<sub>2</sub> = 11.85%.

The RI of sinter is influenced by phase compositions. As shown in Figure 10, the tendency of RI decreases with increasing TiO<sub>2</sub> content. Based on the XRD analysis, the reduction of iron oxides and Ti-bearing iron oxides are carried out in the reduction process. Hence, the reduction reactions of iron oxides and titanium oxides are obstructed due to the nonreactive minerals with increasing TiO<sub>2</sub> content. With the increase of TiO<sub>2</sub> content, the iron grade and the quantity of iron-bearing minerals decrease while gangue minerals of perovskite and Ti-bearing spinel Mg<sub>2</sub>TiO<sub>4</sub> increase. Moreover, under the same reduction condition, the increasing gangue minerals decrease the RI of sinter. Furthermore, combined with the mineral contents of the CVTM sinter with increasing TiO<sub>2</sub> content, the increase of difficultly reductive magnetite, and the decrease of easily reductive hematite and calcium ferrite have negative effects to the RI of CVTM sinter.

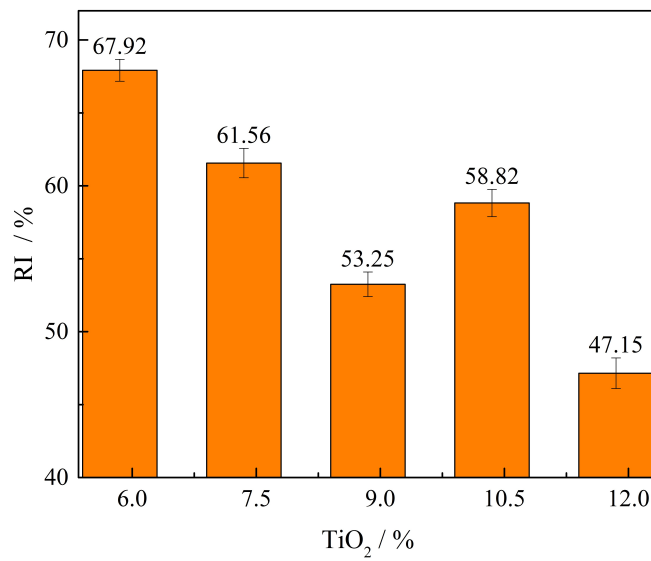


Figure 10. RI of CVTM sinters with different TiO<sub>2</sub> content.

The reduction path of CVTM sinter with CO at 900 °C is shown in Figure 11. The main changes of phases are Fe<sub>3</sub>O<sub>4</sub>, Fe<sub>2.75</sub>Ti<sub>0.25</sub>O<sub>4</sub>, and FeTiO<sub>3</sub>. The phases of CVTM sinter before and after reduction are Fe<sub>3</sub>O<sub>4</sub>, Fe<sub>2</sub>O<sub>3</sub>, MgFe<sub>2</sub>O<sub>4</sub>, CaTiO<sub>3</sub>, and Fe<sub>2</sub>VO<sub>4</sub>. The reduction products of CVTM sinter are Fe, FeO, Mg<sub>2</sub>TiO<sub>4</sub>, TiO, Fe<sub>2.5</sub>Ti<sub>0.5</sub>O<sub>4</sub>, and Fe<sub>2.18</sub>Ti<sub>0.42</sub>O<sub>4</sub>. The main gangue mineral CaTiO<sub>3</sub> increases with the increase of TiO<sub>2</sub> content in the CVTM sinter due to the reaction between FeTiO<sub>3</sub> and CaO in the sintering process of CVTM. The Fe<sub>3</sub>O<sub>4</sub> occupies most of the iron oxides in CVTM sinter, and RDI improves because magnesium ferrite has a suppressing effect on the reduction of hematite with increasing TiO<sub>2</sub> content. The increasing gangue minerals CaTiO<sub>3</sub> and Mg<sub>2</sub>TiO<sub>4</sub> decrease the RI of sinter with increasing TiO<sub>2</sub> content. Hence, TiO<sub>2</sub> addition has favorable effects on low reduction temperature while TiO<sub>2</sub> addition has unfavorable effects on high reduction temperature. The main component difference between VTM and CVTM is the content of Cr<sub>2</sub>O<sub>3</sub>, and the contents of V<sub>2</sub>O<sub>5</sub> and TiO<sub>2</sub> also have differences in the different types of VTM and CVTM. The main differences between sinters of VTM and CVTM are mineral contents of Cr-bearing phase and CaTiO<sub>3</sub> which can affect the quality and performance of the sinter. Compared with the sintering behavior of VTM in our laboratory [9], the RDI of CVTM sinter is superior to VTM sinter due to the suppressing effect of magnesium ferrite, while the RI and TI of CVTM sinter are inferior to VTM sinter due to the more gangue minerals CaTiO<sub>3</sub> in sinter.

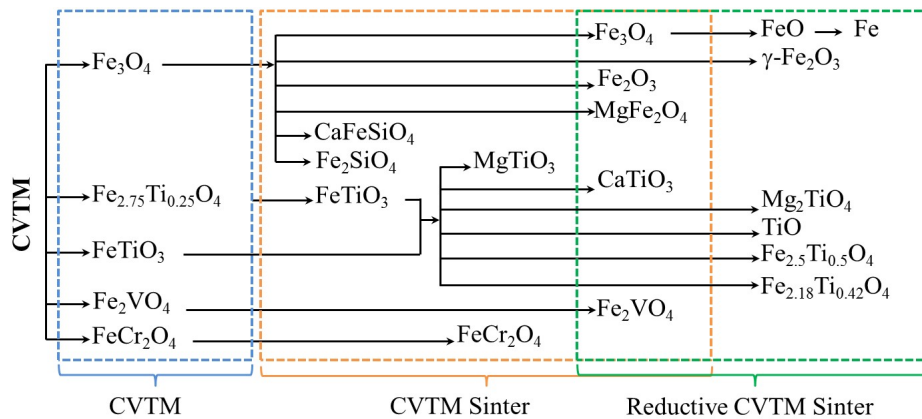
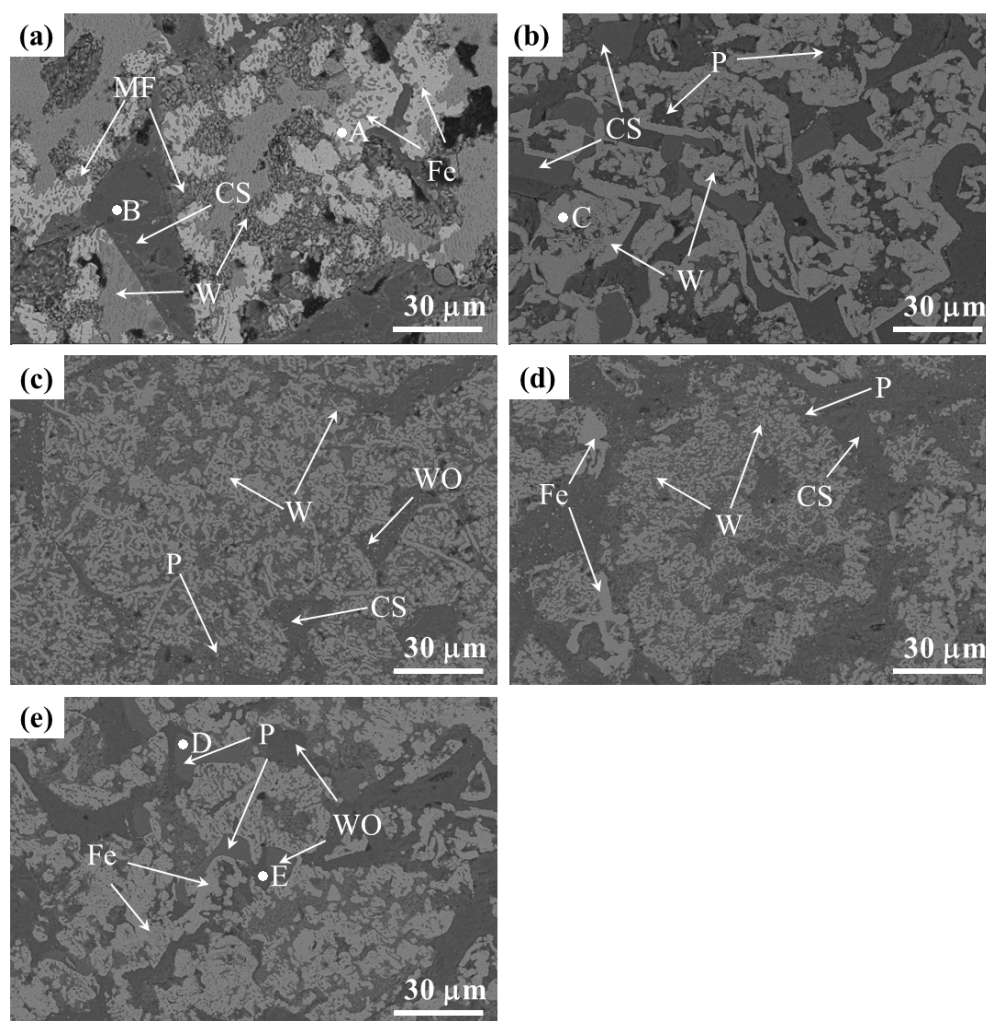


Figure 11. Phase transition path of CVTM sinter.

### 3.3. Microstructure

The investigation of microstructure with different  $\text{TiO}_2$  content on reductive CVTM sinter was analyzed, as shown in Figure 12. Figure 13 presents the corresponding EDS analyses of points A, B, C, D, and E. It can be seen that there are different phases after each reduction, and the different phase boundaries are also easily recognized. An obvious iron phase is observed in light point A in the microstructure, and the contents of O in point A are relatively lower than those in a light grey point C. The silicate phases are also observed in dark grey points B and E. The perovskite phase is observed in a grey point D. With  $\text{TiO}_2$  content in the range of 5.85–7.35%, the subhedral wustite phase concentrates, and perovskite and silicate phase exist among the grains of subhedral wustite and euhedral metallic iron, where the clear boundaries are surrounded by wustite crystals and silicate phase. Meanwhile, pores exist in iron and wustite phases due to the reduction of iron oxides and the aggregation of iron, and many micropores exist in wustite phases, and the porous structure is beneficial in improving the reducing property of the CVTM sinter although this structure is adverse to the sinter strength and RDI. With  $\text{TiO}_2$  content higher than 8.85%, the wustite phase exists dispersively in silicate and perovskite phases. The silicate and perovskite phases obstruct the reduction reactions between reduction gas and wustite. Therefore, the reduction of CVTM sinter decreases with increasing  $\text{TiO}_2$  content. Nevertheless, the relatively uniform structure is beneficial to enhance the strength and RDI of the CVTM sinter in low reduction temperatures.



**Figure 12.** Backscattering detector (BSE) images of reductive CVTM sinter with different  $\text{TiO}_2$  content. W: Wustite; MF: Magnesium Ferrite; CS: Calcium Silicate; P: Perovskite; WO: wollastonite. (a)  $\text{TiO}_2 = 5.85\%$ ; (b)  $\text{TiO}_2 = 7.35\%$ ; (c)  $\text{TiO}_2 = 8.85\%$ ; (d)  $\text{TiO}_2 = 10.35\%$ ; (e)  $\text{TiO}_2 = 11.85\%$ .

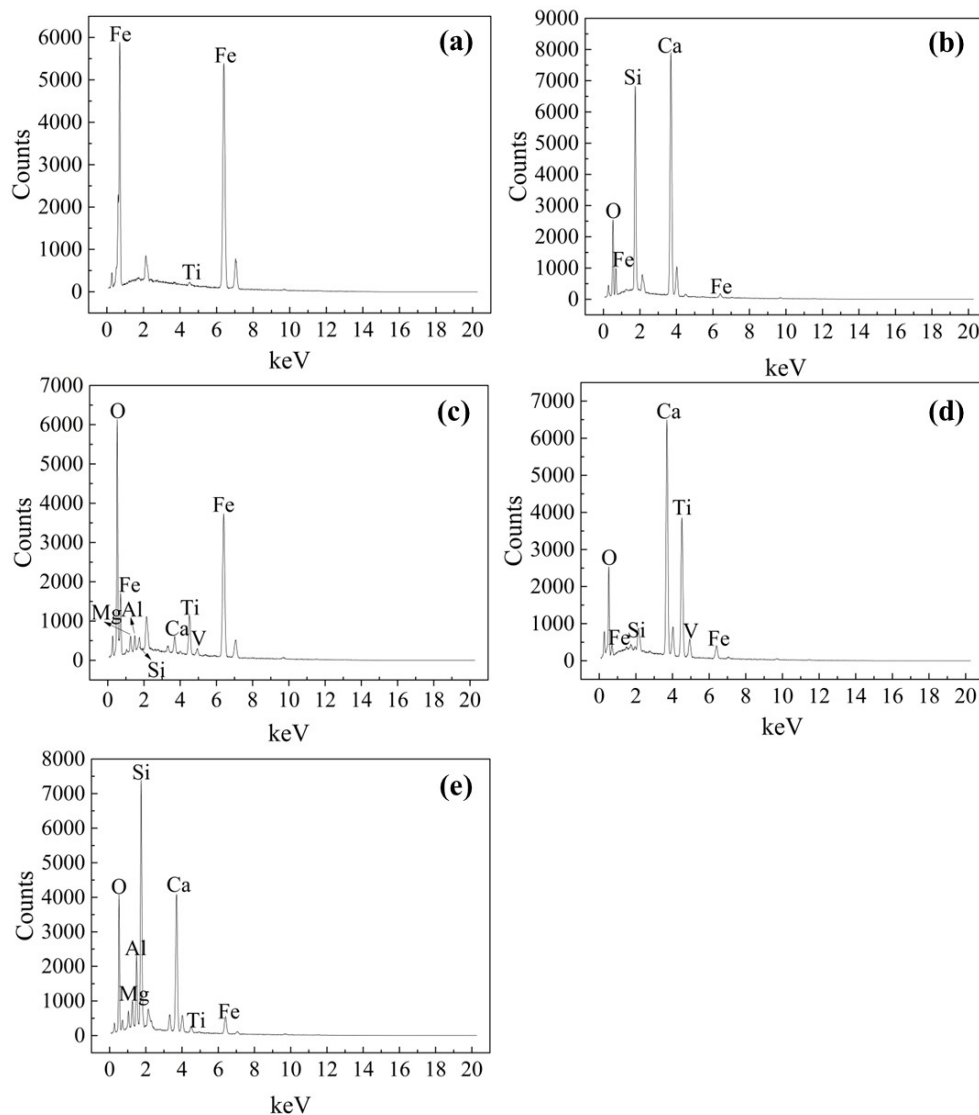


**Figure 13.** Energy disperse spectroscopy (EDS) analyses of different points: (a) point A; (b) point B; (c) point C; (d) point D; (e) point E.

#### 4. Conclusions

The effect of  $\text{TiO}_2$  on the sintering behavior of CVTM sinter was researched. The research contents including yield, TI, vertical sintering speed, productivity, RDI, and RI were studied. Some conclusions were revealed as follows:

- (1) The yield, vertical sintering speed, and productivity first rise with  $\text{TiO}_2$  content increases to 10.35% and then decreases when  $\text{TiO}_2$  content increases to 11.85%. The RI decreases from 67.92% to 47.15% with increasing  $\text{TiO}_2$  content. The principal effect on productivity value is sintering speed.
- (2) The TI increases from 45.81% to 52.09%, and the RDI increases from 74.99% to 96.74% with increasing  $\text{TiO}_2$  content. The RDI of CVTM sinter is well qualified, and the permeability of lumpy zone could be improved with the application of CVTM sinter on BF.
- (3) The main phases of reductive CVTM sinter are metallic iron, wustite, magnesium ferrite, perovskite, coulsonite, spinel  $\text{Mg}_2\text{TiO}_4$ , titanium monoxide, titanomagnetite, and titanomaghemite.

**Author Contributions:** W.T., S.Y., G.C., Z.G., and X.X. contributed to the sintering pot test; W.T. and S.Y. contributed to data analysis and wrote the paper; W.T., H.Y., and X.X. contributed to the design of the experiment.

**Funding:** This research was supported by the National Basic Research Program of China (973 Program) (No. 2013CB632603), and the National Key Technology R&D Program (No. 2015BAB19B02), and the National Natural Science Foundation of China (Nos. 51674084, 51174051 and 51574082).

**Acknowledgments:** This research was financially supported by the National Basic Research Program of China (973 Program) (No. 2013CB632603), and the National Key Technology R&D Program (No. 2015BAB19B02), and the National Natural Science Foundation of China (Nos. 51674084, 51174051 and 51574082).

**Conflicts of Interest:** The authors declare no conflict of interest.

## References

1. Takano, C.; Zambrano, A.P.; Nogueira, A.E.A.; Mourao, M.B.; Iguchi, Y. Chromites reduction reaction mechanisms in carbon-chromites composite agglomerates at 1773K. *ISIJ Int.* **2007**, *47*, 1585–1589. [[CrossRef](#)]
2. Lu, C.Y.; Zou, X.L.; Lu, X.G.; Xie, X.L.; Zheng, K.; Xiao, W.; Cheng, H.W.; Li, G.S. Reductive kinetics of panzhihua ilmenite with hydrogen. *Trans. Nonferr. Met. Soc.* **2016**, *26*, 3266–3273. [[CrossRef](#)]
3. Cheng, G.J.; Xue, X.X.; Gao, Z.X.; Jiang, T.; Yang, H.; Duan, P.N. Effect of Cr<sub>2</sub>O<sub>3</sub> on the reduction and smelting mechanism of high-chromium vanadium-titanium magnetite pellets. *ISIJ Int.* **2016**, *56*, 1938–1947. [[CrossRef](#)]
4. Jena, B.C.; Dresler, W.; Reilly, I.G. Extraction of titanium, vanadium and iron from titanomagnetite deposits at pipestone lake, manitoba, canada. *Miner. Eng.* **1995**, *8*, 159–168. [[CrossRef](#)]
5. Cheng, G.; Gao, Z.; Yang, H.; Xue, X. Effect of calcium oxide on the crushing strength, reduction, and smelting performance of high-chromium vanadium–titanium magnetite pellets. *Metals* **2017**, *7*, 181. [[CrossRef](#)]
6. Cheng, G.J.; Xue, X.X.; Jiang, T.; Duan, P.N. Effect of TiO<sub>2</sub> on the crushing strength and smelting mechanism of high-chromium vanadium–titanium magnetite pellets. *Metall. Trans. B* **2016**, *47*, 1713–1726. [[CrossRef](#)]
7. Yang, S.T.; Zhou, M.; Tang, W.D.; Jiang, T.; Xue, X.X.; Zhang, W.J. Influence of coke ratio on the sintering behavior of high-chromium vanadium–titanium magnetite. *Minerals* **2017**, *7*, 107. [[CrossRef](#)]
8. Yang, S.T.; Tang, W.D.; Zhou, M.; Jiang, T.; Xue, X.X.; Zhang, W.J. Effects of dolomite on mineral compositions and metallurgical properties of chromium-bearing vanadium–titanium magnetite sinter. *Minerals* **2017**, *7*, 210. [[CrossRef](#)]
9. Yang, S.T.; Zhou, M.; Jiang, T.; Wang, Y.J.; Xue, X.X. Effect of basicity on sintering behavior of low-titanium vanadium–titanium magnetite. *Trans. Nonferr. Met. Soc.* **2015**, *25*, 2087–2094. [[CrossRef](#)]
10. Umadevi, T.; Nelson, K.; Mahapatra, P.C.; Prabhu, M.; Ranjan, M. Influence of magnesia on iron ore sinter properties and productivity. *Ironmak. Steelmak.* **2009**, *36*, 515–520. [[CrossRef](#)]
11. Yin, Z.K.; Li, J.S.; Yang, S.F. Sintering pot test on improving TiO<sub>2</sub>-containing ore's allocated proportion. *Adv. Mater. Res.* **2011**, *311–313*, 850–853. [[CrossRef](#)]
12. Xue, M.; Guo, X. Effect of Al<sub>2</sub>O<sub>3</sub> and SiO<sub>2</sub> on formation and crystal structure of calcium ferrite containing Al<sub>2</sub>O<sub>3</sub> and SiO<sub>2</sub>. *J. Chin. Rare Earth Soc.* **2008**, *26*, 205.
13. Zhang, G.L.; Wu, S.L.; Su, B.; Que, Z.G.; Hou, C.G.; Jiang, Y. Influencing factor of sinter body strength and its effects on iron ore sintering indexes. *Int. J. Miner. Metall. Mater.* **2015**, *22*, 553–561. [[CrossRef](#)]
14. Wang, Z.; Pinson, D.; Chew, S.; Rogers, H.; Monaghan, B.J.; Pownceby, M.I.; Webster, N.A.S.; Zhang, G. Behavior of New Zealand ironsand during iron ore sintering. *Metall. Trans. B* **2015**, *47*, 330–343. [[CrossRef](#)]
15. Ren, S.; Zhang, J.L.; Wu, L.S.; Su, B.X.; Xing, X.D.; Zhu, G.Y. Effect of TiO<sub>2</sub> on equilibrium phase sinter at oxygen partial pressure of  $5 \times 10^{-3}$  atm. *Ironmak. Steelmak.* **2013**, *41*, 132–137. [[CrossRef](#)]
16. Lu, L.; Holmes, R.J.; Manuel, J.R. Effects of alumina on sintering performance of hematite iron ores. *ISIJ Int.* **2007**, *47*, 349–358. [[CrossRef](#)]
17. Dwarapudi, S.; Ranjan, M. Influence of oxide and silicate melt phases on the RDI of iron ore pellets suitable for shaft furnace of direct reduction process. *ISIJ Int.* **2010**, *50*, 1581–1589. [[CrossRef](#)]
18. Bristow, N.J.; Loo, C.E. Sintering properties of iron ore mixes containing titanium. *ISIJ Int.* **1992**, *32*, 819–828. [[CrossRef](#)]
19. Zhou, M.; Yang, S.T.; Jiang, T.; Xue, X.X. Influence of MgO in form of magnesite on properties and mineralogy of high chromium, vanadium, titanium magnetite sinters. *Ironmak. Steelmak.* **2015**, *42*, 217–225. [[CrossRef](#)]

